DOI: 10.1002/ ((please add manuscript number))
Article type: Full Paper

Lead-Free Perovskite Derivative $Cs_2SnCl_{6-x}Br_x$ Single crystals for Narrowband Photodetectors

Jun Zhou[#], Jiajun Luo[#], Ximing Rong[#], Peijia Wei, Maxim S. Molokeev, Yang Huang, Jing Zhao, Quanlin Liu, Xiuwen Zhang, Jiang Tang, Zhiguo Xia[*]

J. Zhou, P. J. Wei, Prof. J. Zhao, Prof. Q. L. Liu, Prof. Z. G. Xia
The Beijing Municipal Key Laboratory of New Energy Materials and Technologies,
School of Materials Sciences and Engineering, University of Science and Technology Beijing,
Beijing 100083, P. R. China
E-mail: xiazg@ustb.edu.cn

Prof. Z. G. Xia
State Key Laboratory of Luminescent Materials and Devices and Institute of Optical Communication Materials, South China University of Technology, Guangzhou 510641, China

J. J. Luo, Prof. J. Tang
Sargent Joint Research Center, Wuhan National Laboratory for Optoelectronics (WNLO) and School of Optical and Electronic Information, Huazhong University of Science and Technology (HUST), Wuhan 430074, China

X. M. Rong, Yang Huang, Prof. X. W. Zhang
Shenzhen Key Laboratory of Flexible Memory Materials and Devices,
College of Electronic Science and Technology, Shenzhen University,
Shenzhen 518060, P. R. China

X. M. Rong, Yang Huang
Key Laboratory of Optoelectronic Devices and Systems of Ministry of Education and Guangdong Province,
College of Optoelectronic Engineering, Shenzhen University,
Shenzhen 518060, P. R. China

Dr. M. S. Molokeev
Laboratory of Crystal Physics, Kirensky Institute of Physics,
Federal Research Center KSC SB RAS,
Krasnoyarsk 660036, Russia
Siberian Federal University,
Krasnoyarsk, 660041, Russia
Department of Physics,
Far Eastern State Transport University,
Khabarovsk, 680021 Russia

[#] The three authors contribute equally to this work.

Keywords: $Cs_2SnCl_{6-x}Br_x$; Tin-based single crystals; Photodetectors

Abstract:

The nontoxic and stable Sn halide perovskites demonstrated a tremendous potential in the field of optoelectronic devices. Here, we report the structure and optical properties of the "defect" perovskites $Cs_2SnCl_{6-x}Br_x$ as well as their use as photodetector materials. Millimeter-sized $Cs_2SnCl_{6-x}Br_x$ single crystal have been grown by the hydrothermal method with the body color continuously tuning from transparent to yellow and finally to dark red. We present narrow-band single-crystal photodetectors using $Cs_2SnCl_{6-x}Br_x$ crystals, which shows a high detectivity ≈ 2.71×10^{10} Jones, with a narrowband photodetection (FWHM ~ 45 nm), and higher ion diffusion barriers. Moreover, the response spectra can be continuously tuned from near violet to orange depending on the variations of the bandgap of the single crystals by changing the halide compositions. The strong surface-charge recombination of the excess carriers near the crystal surfaces produced by short-wavelength light elucidate the narrowband photodetection behavior, which refer to light wavelength significantly smaller than absorption edge. This work provides a new paradigm in the design of nontoxic, stable and high-performance perovskite derivative for optoelectronics applications.

1. Introduction

Recently, lead-based perovskite materials with formula $APbX_3$ (A = Cs, methylammonium; X = Cl, Br, I) have received broad attention for their excellent optical and electronic properties in the field of high-efficiency photovoltaic solar cells,[1] light-emitting diodes,[2] and sensitive photodetectors,[3], and so on. However, the presence of lead and unsatisfied stability against heat and humidity restrict their further applications.[4] An effective method is to replace divalent Pb with tetravalent Sn, forming a molecular salt structure with A_2SnX_6 (X = Cl, Br, I) formula, which is a 50% Sn defect perovskite derivative featuring isolated $[SnX_6]^{2-}$ octahedral.[5] This substitution can not only exhibit long-term stability in air but also sustain the high-symmetry cubic structure with different halogen X (X = Cl, Br, I). Furthermore, it is expected that absorption range of A_2SnX_6 can be simply altered by changing the halogen compositions, which is beneficial to high-performance solar cells and wavelength tunable photodetectors.[6]

Photodetectors that capture light signals and convert them into electric signals are very important functional components in many applications. The majority of photodetectors are non-selective to a wide range of wavelength, however, narrowband photodetection with small full-width at half-maximum (FWHM) of spectral response is extensively used in imaging, surveillance and sensing where either require high spectral resolution or only detect specific wavelength region.[7] The traditional method to realize narrowband photodetection is to combine the broadband photodetector with bandpass filters. However, these filters increase the structure complexity and limit pixel density in imaging system. Filter-free narrowband photodetectors are recently demonstrated in perovskite and perovskite derivative single crystals with narrow response spectrum, high sensitivity as well as tunable from ultraviolet to infrared, exhibiting great potential in filter-free narrowband photodetector application.[8] Here, we report the crystal growth of the millimeter-sized $Cs_2SnCl_{6-x}Br_x$ single crystal, and the body color can be continuously tuned from transparent to yellow and finally to dark red depending

on the varied Cl/Br ratios. Using these single crystals as the photoactive materials in photodetectors, narrowband photodetection model with a tunable response spectral profile from near violet to orange was realized. Low toxicity, high detectivity (2.71×10^{10} Jones), narrowband photodetection (FWHM ~ 45 nm), and higher ion diffusion barriers make our $Cs_2SnCl_{6-x}Br_x$ photodetector a promising candidate for more diverse applications. This is the first example on the nontoxic, stable and high-performance perovskite derivative $Cs_2SnCl_{6-x}Br_x$ for narrowband photodetectors.

2. Results and discussion

Figure 1a shows the orthogonal unit cell structure of $Cs_2SnCl_{6-x}Br_x$ with periodic supercell based on Cs_2SnCl_6. $Cs_2SnCl_{6-x}Br_x$ is a defect variant of the 3-D perovskite $CsSnX_3$, not the bona fide perovskite, which is obtained by removing half of the Sn atoms at each center interval of the [$SnCl/Br_6$] octahedron.[9] Moreover, Cs atoms, which form a regular 12-fold coordination with Cl/Br atoms, are filled in the sites between the [$SnCl/Br_6$] octahedral. Hence, $Cs_2SnCl_{6-x}Br_x$ can be considered as a molecular salt containing Sn^{4+} with high stability and nontoxic elements.[10] Figure 1b shows the photographs of as-grown single crystals of single-halide and mixed-halide compositions, and the body colors can be gradually tuned from transparent to yellow and finally to dark red with increasing x (in $Cs_2SnCl_{6-x}Br_x$) from 0 to 1. Scanning electron microscope (SEM) images were collected to examine the crystal quality of the selected samples (Figure 1c-e for the Cs_2SnCl_6, Cs_2SnBr_6, and $Cs_2SnCl_3Br_3$). There are basically no porosity and any other defects on the artificially cracked fracture surface, which shows that the crystals have very high crystal quality represented by smooth and compact surface. Moreover, the energy dispersive X-ray spectroscopy (EDS) elemental mapping technique was used to confirm the composition uniformity of $Cs_2SnCl_3Br_3$, as shown in Figure 1f-i. The elemental mapping images exhibit that Cs, Sn, Cl and Br are homogeneously distributed within the fracture surface. The XRD patterns of the as-prepared

$Cs_2SnCl_{6-x}Br_x$ samples are given in Figure 1j. It is found that all the diffraction peaks were successfully indexed by cubic cell (*Fm*-3*m*) with parameters close to Cs_2SnCl_6 and Cs_2SnBr_6.[5c] In the meantime, the characteristic diffraction peak (0 2 2) shifts to lower diffraction angles from 24.22° to 23.43° with increasing Br content owing to the different ionic radii between Br^- and Cl^- (Figure 1k), further suggesting that the continuous solid solution of $Cs_2SnCl_{6-x}Br_x$ have been formed. To further determine the actual halide compositions of the crystals, the Rietveld refinement analysis of this series of $Cs_2SnCl_{6-x}Br_x$ has been conducted by using TOPAS 4.2 and Cs_2SnCl_6 was taken as starting model. There is only one Cl site in the structure and it was occupied randomly by Cl^- and Br^- ions in our model. Based on the Rietveld refinement results, all of these samples exhibit the same cubic cell (*Fm*-3*m*). The refinement results of $Cs_2SnCl_{6-x}Br_x$ were stable, and the main processing and refinement parameters, including fractional atomic coordinates, isotropic displacement parameters and main bond lengths are shown in Table S1-3. Thus, the actual halide compositions of the crystals by Rietveld refinement analysis have been also listed in Figure 1j, which roughly matched the Br/Cl ratio in the precursor.

After fully relaxation, the lattice constants (L_c) in theory for Cs_2SnCl_6 and Cs_2SnBr_6 are calculated as 10.74 and 11.25 Å, respectively, which are both close to our experimental measurements of 10.39 and 10.74 Å. The unit cell volumes (V) for $Cs_2SnCl_{6-x}Br_x$ are presented in Figure 1m. The monotonously increases of the V is mainly caused by the radii difference between Cl^- and Br^- during the anion substitution, and is consistent with our experimental tendency. That's to say, both of them obey the Vegard's law with linear variation depending on the changing Cl/Br ratios in $Cs_2SnCl_{6-x}Br_x$. In order to investigate the phase stability of $Cs_2SnCl_{6-x}Br_x$, we calculate the energetics for the formation pathway of $Cs_2SnCl_{6-x}Br_x$:

$$(1-x/6)\ Cs_2SnCl_6 + x/6\ Cs_2SnBr_6 \rightarrow Cs_2SnCl_{6-x}Br_x.$$

Figure 1n shows the calculated formation energy per atom of $Cs_2SnCl_{6-x}Br_x$ as a function of *x*. The formation energies of $Cs_2SnCl_{6-x}Br_x$ solid solution are positive, and also present a quadratic relations as a function of *x*, meaning that the solid solutions have less stable nature than Cs_2SnCl_6 or Cs_2SnBr_6, due to the strain energy from the size mismatch of Cl^- and Br^- constituents. However, the energies for the solid solutions are less than 3.5 meV/atom higher than the stable perovskites, relatively small enough to be overcame by the mixing entropy, suggesting that $Cs_2SnCl_{6-x}Br_x$ could be stabilized at medium temperature. For a theoretical comparison, we further compared the stability of $Cs_2SnCl(Br)_6$ with different space group, as shown in Table S4. For $Cs_2SnCl(Br)_6$, the structures with *Pnma* space group are originated from well-known orthorhombic single perovskite lead-based $CsPbCl_3$. Through atomic substitution of Pb to Sn, Cl to Br, and vacancy making, we got lead-free $CsSnCl(Br)_3$ and $Cs_2SnCl(Br)_6$ orthorhombic structures. For all those originated and processing structures, the energies with *Fm*-3*m* space group are larger than that with *Pnma* space group, suggesting that these materials with *Pnma* could be a more stable phase than *Fm*-3*m* structures at 0 K. However, *Fm*-3*m* could be a stable phase at higher temperature, meaning that the phase transition from *Pnma* to *Fm-3m* structures could occur as the temperature increases. We note that the energy differences between the *Pnma* and *Fm-3m* phases for $Cs_2SnCl(Br)_6$ are neglectable (see Table S4), hinting that these ordered-vacancy materials could be stable in the cubic phase start at 0 K in light of the tolerance of DFT total energy calculations or a very low temperature. The ordered distribution of vacancies in Cs_2SnCl_6 (Cs_2SnBr_6) would require a concert movement of anions around the vacancies as in the cubic *Fm-3m* structure, and would resist the orthorhombic distortion as in *Pnma* phase. The enhanced stability of the cubic phase (*Fm-3m*) relative to the distorted phase (*Pnma*) for Cs_2SnCl_6 and Cs_2SnBr_6, as well as the small mixing formation energy (3.5 meV/atom) between them enables the continuously tunable composition and thus different bandgap values as discussed below.

To demonstrate optical band gaps for these materials, the UV-Vis diffuse reflection data have been collected. As shown in Figure 2a, with increasing Br/Cl ratio, the as-measured spectra of $Cs_2SnCl_{6-x}Br_x$ show a gradually redshifted absorption edge, which matches well with their body colors. And the band gap values in the $Cs_2SnCl_{6-x}Br_x$ can be estimated according to eq 1[11]

$$[F(R_\infty)h\nu]^n = A\,(h\nu - E_g)$$

where $h\nu$ is the photon energy; A is a proportional constant; E_g is the value of the band gap; n = 2 for a direct transition or 1/2 for an indirect transition; and $F(R_\infty)$ is the Kubelka-Munk function defined as[11]

$$F(R_\infty) = (1-R)^2/2R = K/S$$

where R, K, and S are the reflection, absorption, and scattering coefficient, respectively. From the linear extrapolation of $[F(R_\infty)h\nu)^2] = 0$, we can estimate a direct optical band gap value of a crystal compound, and the values of 4.66, 4.63, 4.60, 4.42, 4.03, 3.77, 3.59, 3.55, 3.51, 3.40 and 3.34 eV were obtained for x = 0, 0.23 (2), 0.52 (2), 0.89 (2), 1.14 (2), 1.75 (2), 3.03 (3), 3.32 (3), 3.43 (3), 3.65 (3), 6 , respectively (Figure 2b). Thus, in $Cs_2SnCl_{6-x}Br_x$ compounds, the bandgap values decreases obviously with the increasing x. Figure 2c and 2d show the calculated band structures for Cs_2SnCl_6 and Cs_2SnBr_6 by both PBE and HSE approaches. For both Cs_2SnCl_6 and Cs_2SnBr_6, the bands show direct band gap, with VBM and CBM both located at Γ (0, 0, 0). The calculated HSE/PBE band gap for Cs_2SnCl_6 and Cs_2SnBr_6 are 3.99/2.66 and 2.51/1.44 eV, respectively, which corresponds to the experimental measurement of 4.46 and 3.34 ev, and they are consistent with the calculation method of HSE reported by Dalpian et. al.[12] The HSE and PBE band structures for $Cs_2SnCl_{6-x}Br_x$ (x = 1 ~ 5) were presented in Figure S2 and Figure S3, respectively. For all procedure of Cl^-~Br^- transition, VBM and CBM remain locating at Γ (0, 0, 0), indicating direct gap for all structures. Details of band gaps are presented in Figure 2b, as the band gaps for $Cs_2SnCl_{6-x}Br_x$

alloys decrease as *x* increases from 0 to 6. Such variation tendency of band gap is in agreement with the experimental observations.

To further evaluate the optoelectronic properties of $Cs_2SnCl_{6-x}Br_x$, a photoconductive photodetector device is fabricated by thermally evaporating gold onto opposite sides (one side 30 nm, and the other side 100 nm) of $Cs_2SnCl_{6-x}Br_x$ crystals, as schemed in Figure 3a. Note that one side with thin gold (~30 nm) was used to minimize the light absorbed by metal. Since the optical field distribution in the crystals conforms to the Beer-Lambert Law, the light penetration length (I_p) is strongly covalent with the extinction coefficient. Short wavelength light, which refers to light wavelength significantly smaller than the absorption edge, gives a high extinction coefficient and short I_P (as illustrated in Figure 3b), thus the carriers generated by short wavelength light is mainly near the Au/crystal interface (generally < 300 nm), where surface charge recombination occur. Photo generated carriers diffuse quickly (within the range of electron diffusion length I_e) and be trapped by the surface defects ($I_P \leqslant I_e$), and these carriers cannot be collected and contribute to photocurrent. Meanwhile, carriers generated by long wavelength light with longer I_P can be driven toward positive electrode by applied electric field (drift length I_D), exhibiting less surface charge recombination and higher collection efficiency (as illustrated in Figure 3b). One can also find some details on such a similar photodetection mechanism in the previous work.[7]

Figure 3c showed the dynamic current-time (I–t) photoresponse under the repetitive switching of different wavelength monochromatic illumination at a bias of -20 V. Both the dark current and photocurrent are steady and repeatable under the high voltage, indicating weak ion migration in $Cs_2SnCl_{6-x}Br_x$ crystals. The response spectra is measured by the wavelength-dependent external quantum efficiency (EQE) of the $Cs_2SnCl_{6-x}Br_x$ photodetectors (Figure 3d), which exhibit a single narrow peak close to the absorption edge of each kind of single crystal, exhibiting negligible photoresponse to wavelength either larger nor significantly smaller than the absorption edge. The narrow photodetecotion peaks are also

red-shifted with the increasing *x*, in accordance with the absorption edge, and the detail devices data of different Cl/Br ratios is also shown in the Figure S4.

The photodetection capability of the narrowband photodetectors was measured and evaluated. Figure 4a exhibits the dark current and photocurrent under the light intensity of 1.27 mW cm^{-2}, and their linear feature indicate a good ohmic contact of Au/ perovskite derivative. The resistivity of Cs_2SnBr_6 was calculated to be as high as 3×10^{11} Ω, which may attribute to few shallow trap density and high crystal quality. The photo response time is obtained by measuring the 3 dB cut-off frequency values, and the obtained -3 dB point at -10 V and -20 V were 105 Hz (9.52 ms) and 230 Hz (4.34 ms), respectively (Figure 4b). The normalized detectivity can be used to evaluate the ability to detect weak light of various photodetectors, as calculated by the following equation:

$$D^* = (Af)^{1/2} R / i_n$$

where *A* is the effective area of the detector, *f* is the electrical bandwidth and i_n is the noise current. Here, the noise current is directly measured by the low noise current amplifier and the output connect to lock-in amplifier. As shown in Figure 4c, the measured noise current of the Cs_2SnBr_6 crystal is barely sensitive to frequency, indicating a negligible 1/f noise of our devices due to the relatively high crystal quality of our Cs_2SnBr_6 crystal. The calculated D^* of devices was 2.71×10^{10} Jones with narrowband photodetection (FWHM ~ 45 nm) (Figure 4d), which is comparable with the $MAPbX_3$ (Cl, Br, I) crystal based devices.[7]

We further applied first-principles calculations to simulate the diffusion barrier for three types of ions (Cs^+, Sn^{4+}, $Cl^-/(Br^-)$) in $Cs_2SnCl(Br)_6$ via vacancy-assisted diffusion: V_{Cs}, V_{Sn} and $V_{Cl/(Br)}$, respectively, as shown in Figure 4e (for Cs_2SnCl_6) and 4f (for Cs_2SnBr_6). According to the results, $V_{Cl/(Br)}$ was found to have the lowest diffusion barrier of ~ 0.33 (0.23) eV and the shortest migration distance among all vacancies, comparable with the diffusion barriers V_{Br} calculated for $MAPbBr_3$ (~0.2 eV)[13] and $Cs_2AgBiBr_6$ (0.33 eV)[14]

elsewhere. For halide perovskites, ion diffusion barriers are highly dependent on the movement of nearby molecules or ions along diffusion pathway. As for the organic–inorganic hybrid perovskite, there is more freedom for structural relaxation due to the orientation and rotation of nearby molecules to release strain energies during diffusion. In $A_2B^+C^{3+}X_6$ double perovskite structure (take $Cs_2AgBiBr_6$ for example), the interactions for a collinear Ag^+-Br^--Bi^{3+} could cause the constraint of Br^- less than single Ag^+-Br^- of Ag^+-Br^- interactions. In such as case for $Cs_2SnCl(Br)_6$, $Cl^-(Br^-)$ ions were connected by a Sn^{4+} cation and a vacancy site. Such unique structural configuration gives more freedom to $Cl^-(Br^-)$ ions for ion diffusion comparing with $A_2B^+C^{3+}X_6$ structure, but the constraint is still larger than $MAPbBr_3$, as indicated by the diffusion barriers. Such diffusion difficulty will be presented to be better stability and higher ion diffusion barriers comparing with $MAPbBr_3$, as observed for Cs_2SnCl_6 and Cs_2SnBr_6 in this work, which is further confirmed by comparing the dark current baseline of $MAPbBr_3$ and Cs_2SnBr_6 under high electric bias (Figure 5a).[13] Moreover, the responsivity of the photodetector over time is shown in Figure 5b, and the device performance can be maintained almost 90% of its initial value after storage in 60% relative humidity conditions for 20 days.

3. Conclusion

In summary, millimeter-sized $Cs_2SnCl_{6-x}Br_x$ single crystal have been grown by the hydrothermal method, and we have successfully realized narrowband photodetection by perovskite derivative $Cs_2SnCl_{6-x}Br_x$ single-crystal photodetectors. The response spectra can be continuously tuned from near violet to orange by changing the halide compositions in the single crystals. The narrowband photodetection can be explained by the strong surface-charge recombination-induced suppression of charge collection for short-wavelength excitation. Low toxicity, high detectivity (2.71×10^{10} Jones), narrowband photodetection (FWHM ~ 45 nm), and

higher ion diffusion barriers make our $Cs_2SnCl_{6-x}Br_x$ photodetector a strong candidate for more diverse applications. It is reasonable to expect that the solution growth of perovskite derivative single crystals can be extended to the preparation, compositions design and manipulation of optical properties of other high-performance, lead-free, and stable photodetector materials.

Experimental Section

Materials and Preparation: All the chemicals were commercially purchased and used without further purification. Crystals $Cs_2SnCl_{6-x}Br_x$ were synthesized by the hydrothermal method in a stainless steel Parr autoclave using CsCl (99.99%, Aladdin) and $SnCl_2$ (99.99%, Aladdin) in the haloid acid solution at different HCl (A. R., Beijing Chemical Works)/HBr (A. R., Beijing Chemical Works) ratios. Large $Cs_2SnCl_{6-x}Br_x$ crystals (as shown in Figure 1b) can be grown from the solution upon heating at 453 K for 36 h and then slowly decreased to room temperature. These crystals were filtered out and then washed with ethanol and finally dried at 60 ^oC under a vacuum drying oven overnight. The $MAPbBr_3$ crystals growth method is reported by Prof. Huang.[15]

Characterization: The powder X-ray diffraction (XRD) measurements were conducted on a D8 Advance diffractometer (Bruker Corporation, Germany) operating at 40 kV and 40 mA with Cu Kα radiation (λ = 0.15406 Å), and the scanning rate was fixed at 4^o/min. The powder diffraction pattern for Rietveld analysis was collected with the same diffractometer. The step size of 2θ was 0.016^o, and the counting time was 1 s per step. Rietveld refinement was performed by using TOPAS 4.2 software.[16] The crystal morphology was characterized by scanning electron microscope (SEM, JEOL JSM-6510). The diffuse reflectance spectra were measured on a UV-Vis-NIR spectrophotometer (SHIMADZU UV-3600) supplied with an integrating sphere.

Computational method: For theoretical details, all first-principles calculations were performed based on the density functional theory (DFT), as implemented in the Vienna *ab*

initio simulation package (VASP) code.[17] The projector augmented wave (PAW) potential method [18] was used to describe the interactions between ions and electrons, and the exchange–correlation interactions between electrons were treated within the generalized gradient approximation (GGA–PBE).[19] The plane wave cut-off energy of 500 eV was used for all structural optimizations and electronic calculations. The K-point meshes were generated according to the Monkhorst–Pack scheme[20] for the Brillouin zones, as Γ-centered with a k-grid density of $0.02 \times 2\ \pi$ Å^{-1} for ionic interactions and electronic SCF interactions. The convergence criterion for the energy in electronic SCF iterations and the force in ionic step iterations were set to 1.0×10^{-6} eV and 1.0×10^{-2} eV Å^{-1}, respectively. To reduce the self-interaction error of DFT in band gap calculations, we also used Heyd-Scuseria-Ernzerhof (HSE) hybrid functional approach[21] to evaluate the band gap and to compare with the PBE functional approach. Calculations for diffusion barrier was applied using the method mentioned in Ref.[14]

Devices fabrication and characterization: The photoconductive detectors were fabricated by thermally evaporating (Fangsheng Technology, OMV-FS300) Au electrodes on the opposite side of the crystal under 1 x 10^{-5} mTorr. Note that the thickness of the thin layer of Au is about 30 nm to form a semitransparent anode. For devices performance characterization, all the measurements were carried out in an optically and electrically sealed box. The photo response was recorded by Agilent B1500A at given voltage. The wavelength dependent response spectra was measured by modulating a bromine tungsten lamp using optical grating with a minimum interval of 5 nm. The monochromatic light source of dynamic current-time (I-t) photoresponse was a given wavelength LED (Thorlabs) modulated by a waveform generator (Agilent 33600A Series). The light intensity applied for all the measurements was measured by Newport 1916-R Optical Power Meter. The device was bias by low noise current amplifier (SR570) and the output was connect to lock-in amplifier (SR850). SR570 was work in high bandwidth mode (High BW) without added any filter.

Supporting Information
Supporting Information is available from the Wiley Online Library or from the author.

Acknowledgements
The present work was supported by the National Natural Science Foundation of China (Grants 51722202, 91622125, 51572023, and 11774239), Natural Science Foundations of Beijing (2172036), and National Key R&D Program of China Grant No. 2016YFB0700700.

Received: ((will be filled in by the editorial staff))
Revised: ((will be filled in by the editorial staff))
Published online: ((will be filled in by the editorial staff))

References

[1] M. Saliba, T. Matsui, K. Domanski, J. Y. Seo, A. Ummadisingu, S. M. Zakeeruddin, J. P. Correa-Baena, W. R. Tress, A. Abate, A. Hagfeldt, M. Grätzel, *Science.* **2016**, 354, 206.

[2] Y. H. Kim, H. Cho, J. H. Heo, T. S. Kim, N. Myoung, C. L. Lee, S. H. Im, T. W. Lee, *Adv. Mater.* **2015**, 27, 1248.

[3] a) L. Dou, Y. M. Yang, J. B. You, Z. R. Hong, W. H. Chang, G. Li, Y. Yang, *Nat. Commun.* **2014**, 5, 5404; b) M. I. Saidaminov, V. Adinolfi, R. Comin, A. L. Abdelhady, W. Peng, I. Dursun, M. J. Yuan, S. Hoogland, E. H. Sargent, O. M. Bakr, *Nat. Commun.* **2015**, 6, 8724.

[4] X. G. Zhao, J. H. Yang, Y. H. Fu, D. W. Yang, Q. L. Xu, L. P. Yu, S. H. Wei, L. J. Zhang, *J. Am. Chem. Soc.* **2017**, 139, 2630.

[5] a) B. Lee, C. C. Stoumpos, N. J. Zhou, F. Hao, C. Malliakas, C. Y. Yeh, T. J. Marks, M. G. Kanatzidis, R. P. H. Chang, *J. Am. Chem. Soc.* **2014**, 136, 15379; b) B. Saparov, J. P. Sun, W. W. Meng, Z. W. Xiao, H. S. Duan, O. Gunawan, D. Shin, I. G. Hill, Y. F. Yan, D. B. Mitzi, *Chem. Mater.* **2016**, 28, 2315; c) A. Kaltzoglou, M. Antoniadou, A. G. Kontos, C. C. Stoumpos, D. Perganti, E. Siranidi, V. Raptis, K. Trohidou, V. Psycharis, M. G. Kanatzidis, P. Falaras, *J. Phys. Chem. C.* **2016**, 120, 11777.

[6] a) J. K. Jiang, C. K. Onwudinanti, R. A. Hatton, P. A. Bobbert, S. X. Tao, *J. Phys. Chem. C.* **2018**, 122, 17660; b) M. Konstantakou, T. Stergiopoulos, *J. Mater. Chem. A.* **2017**, 5, 11518.

[7] Y. J. Fang, Q. F. Dong, Y. C. Shao, Y. B. Yuan, J. S. Huang, *Nat. Photonics.* **2015**, 9, 679.

[8] Z. Zheng, F. W. Zhuge, Y. G. Wang, J. B. Zhang, L. Gan, X. Zhou, H. Q. Li, T. Y. Zhai, *Adv. Funct. Mater.* **2017**, 27, 1703115.

[9] Z. F. Tan, J. H. Li, C. Zhang, Z. Li, Q. S. Hu, Z. W. Xiao, T. Kamiya, H. Hosono, G. D. Niu, E. Lifshitz, Y. B. Cheng, J. Tang, *Adv. Funct. Mater.* **2018**, 1801131.

[10] A. F. Wang, X. X. Yan, M. Zhang, S. B. Sun, M. Yang, W. Shen, X. Q. Pan, P. Wang, Z. T. Deng, *Chem. Mater.* **2016**, 28, 8132.

[11] J. Zhou, Z. G. Xia, M. S. Molokeev, X. W. Zhang, D. S. Peng, Q. L. Liu, J. Mater. Chem. A. **2017**, 5, 15031.

[12] G. M. Dalpian, Q. Liu, C. C. Stoumpos, A. P. Douvalis, M. Balasubramanian, M. G. Kanatzidis, A. Zunger, *Phys. Rev. Mater.* **2017**, 1, 025401.

[13] S. Meloni, T. Moehl, W. Tress, M. Franckevicius, M. Saliba, Y. H. Lee, P. Gao, M. K. Nazeeruddin, S. M. Zakeeruddin, U. Rothlisberger, M. Graetzel, *Nat. Commun.* **2016**, 7, 10334.

[14] W. C. Pan, H. D. Wu, J. J. Luo, Z. Z. Deng, C. Ge, C. Chen, X. W. Jiang, W. J. Yin, G. D. Niu, L. J. Zhu, L. X. Yin, Y. Zhou, Q. G. Xie, X. X. Ke, M. L. Sui, J. Tang, *Nat. Photonics.* **2017**, 11, 726.

[15] H. T. Wei, Y. J. Fang, P. Mulligan, W. Chuirazzi, H. H. Fang, C. C. Wang, B. R. Ecker, Y. L. Gao, M. A. Loi, L. Cao, J. S. Huang, *Nat. Photonics.* **2016**, 10, 333.

[16] V. TOPAS, Bruker AXS: Karlsruhe, Germany. **2008**.

[17] a) G. Kresse, J. Furthmuller, *Comput. Mater. Sci.* **1996**, 6, 15; b) G. Kresse, J. Furthmuller, *Phys. Rev. B.* **1996**, 54, 11169.

[18] P. E. Blöchl, *Phys. Rev. B.* **1994**, 50, 17953.

[19] J. P. Perdew, K. Burke, M. Ernzerhof, *Phys. Rev. Lett.* **1996**, 77, 3865.

[20] D. J. Chadi, *Phys. Rev. B.* **1977**, 16, 1746.

[21] A. V. Krukau, O. A. Vydrov, A. F. Izmaylov, G. E. Scuseria, *J. Chem. Phys.* **2006**, 125, 224106.

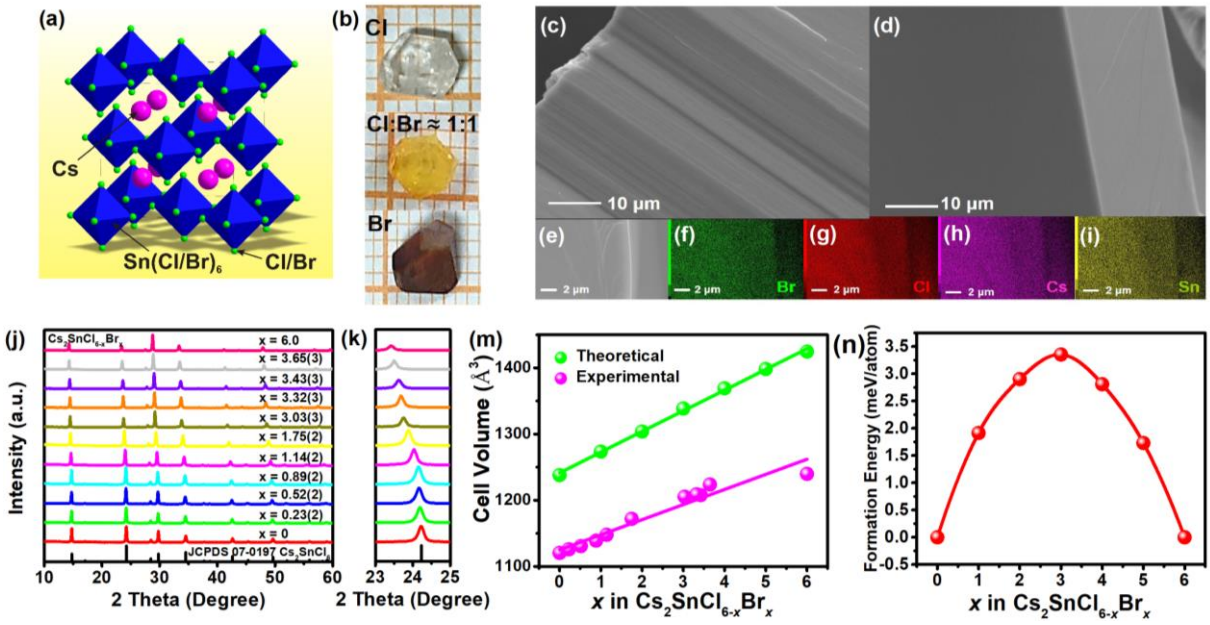

Figure 1. a) Three-dimensional crystal structure diagram of defect perovskites $Cs_2SnCl_{6-x}Br_x$, and half of the octahedral Sn atoms are missing, creating discrete $[Sn(Cl,Br)_6]^{2-}$ octahedra. b) Photographs of single-halide and mixed-halide $Cs_2SnCl_{6-x}Br_x$ single crystals with body colors changing from transparent to yellow and finally to dark red. SEM images of the artificially cracked fracture surface of Cs_2SnCl_6 c), Cs_2SnBr_6 d), and $Cs_2SnCl_3Br_3$ e). f)-i) Element mapping images of Br, Cl, Cs and Sn for the selected $Cs_2SnCl_3Br_3$ crystal. j) XRD patterns and k) selected diffraction peaks near 24° of the as-prepared $Cs_2SnCl_{6-x}Br_x$ (x = 0 – 6.0). m) Theoretical and experimental unit cell volume V of $Cs_2SnCl_{6-x}Br_x$ samples as a function of x. n) Calculated formation energies per atom of $Cs_2SnCl_{6-x}Br_x$ as a function of x.

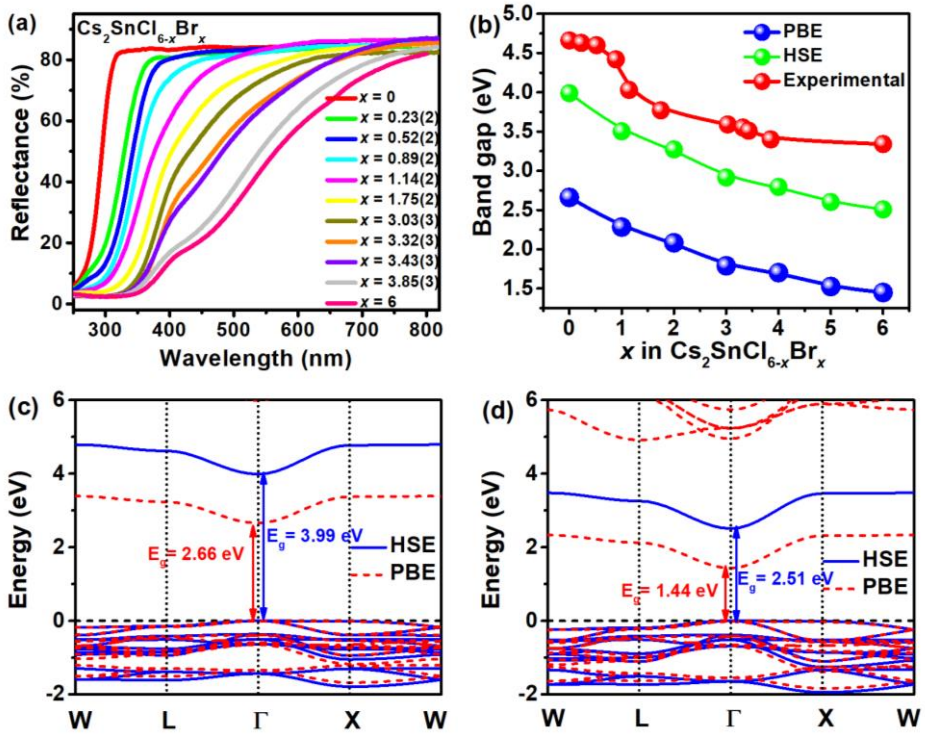

Figure 2. a) UV-vis diffuse reflectance spectra and b) the band gap changing map for $Cs_2SnCl_{6-x}Br_x$ (x = 0 - 6.0) depending on different halide compositions. Calculated electronic

band structures of c) Cs_2SnCl_6 and d) Cs_2SnBr_6 from the PBE and HSE calculations with SOC.

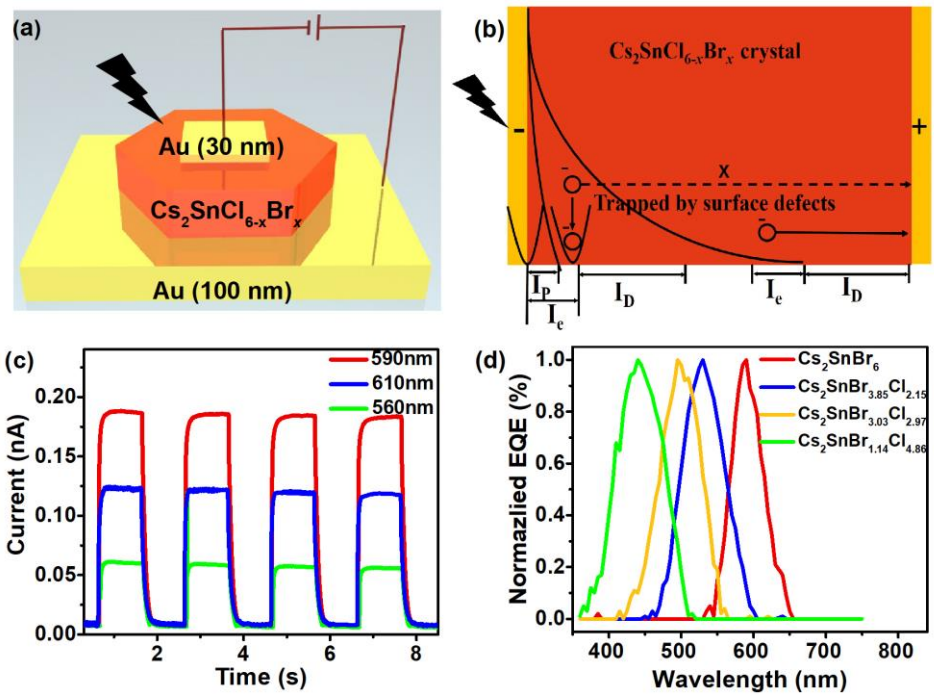

Figure 3. a) Schematic diagram of $Cs_2SnCl_{6-x}Br_x$ based device structure. b) The mechanism for narrowband photodetector, and I_p, I_e, I_D refer to penetration length, electron diffusion length, drift length, respectively. c) Temporal response with -20 V bias under different wavelength LED illumination (590 nm, 610 nm and 560 nm respectively) with the same light intensities of 1.3 $mWcm^{-2}$ and a modulation frequency of 125 mHz. d) Normalized EQE spectra of $Cs_2Sn(Br,Cl)_6$ based single crystal photodetectors with different halide compositions, and he EQE spectra were measured under -20 V bias.

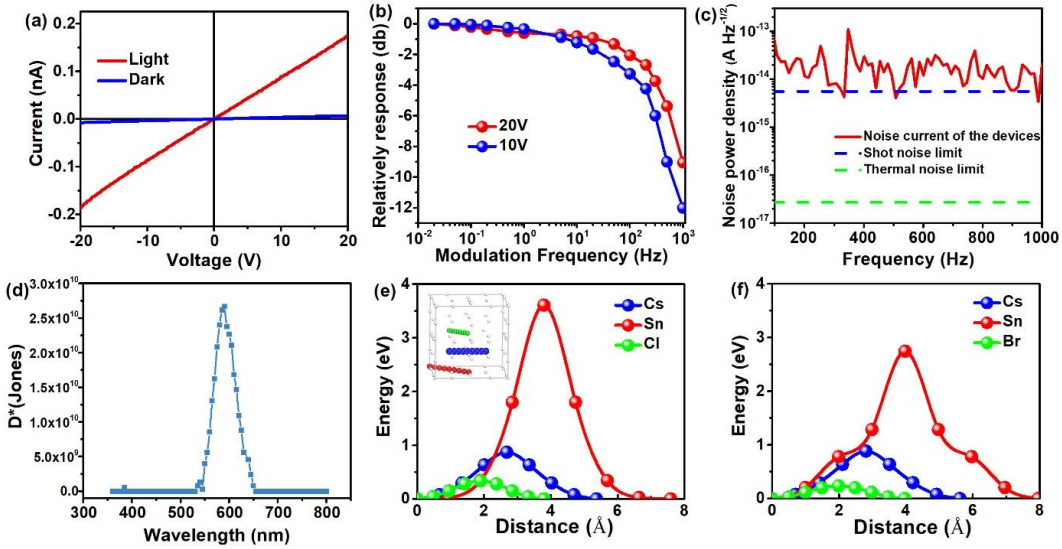

Figure 4. a) The current−voltage curve of typical Cs_2SnBr_6 crystal detector both in dark and under 590 nm monochromatic light LED with the intensities of 1.3 $mWcm^{-2}$. b) Normalized response of the Cs_2SnBr_6 crystal detector *vs* the input signal frequency (light intensity of 1.3 mW cm^{-2}) at a bias voltage of -20 V. c) Measured total current noise of the Cs_2SnBr_6 crystal detector at various frequencies under the bias of -20 V. d) Specific detectivity (D*) spectrum of the Cs_2SnBr_6 crystal detector under -20V bias. Calculated energy profile along the ionic

migration path for the possible ion vacancies in Cs_2SnCl_6 e) Cs_2SnBr_6 f). Inset in (e): Migration path of these ion vacancies.

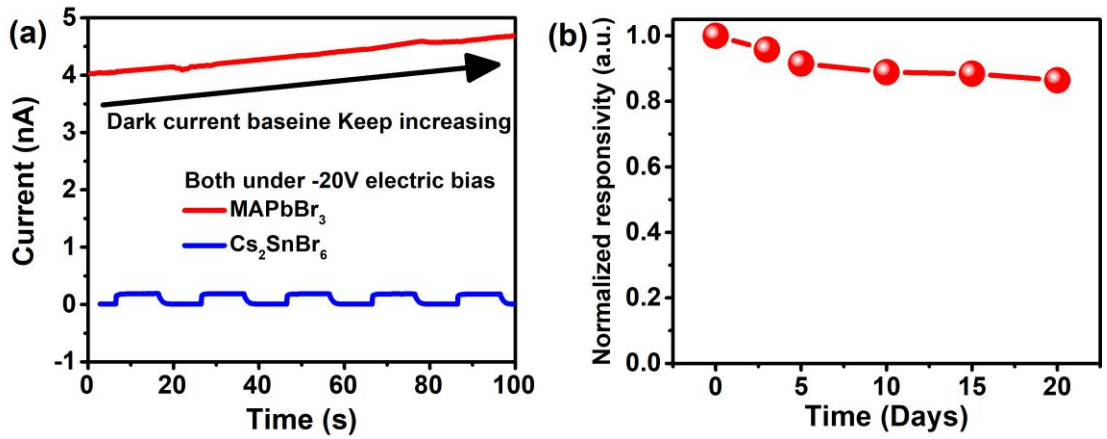

Figure 5. a) Device stability test of Cs_2SnBr_6 crystal from the comparison of the curves of $MAPbBr_3$ crystal (1.4 mm in thickness) and Cs_2SnBr_6 crystal (1.3 mm in thickness) under constant -20 V electric bias, respectively. b) Normalized responsivity measurement of Cs_2SnBr_6 crystal-based device with the storage under ~ 60% relative humidity after a certain time intervals.

Table of Contents entry

Millimeter-sized $Cs_2SnCl_{6-x}Br_x$ single crystal have been grown, and the narrow-band single-crystal photodetectors using $Cs_2SnCl_{6-x}Br_x$ crystals show a high detectivity ≈ 2.71×10^{10} Jones, with a narrowband photodetection (FWHM ~ 45 nm), and higher ion diffusion barriers. This work provides a new paradigm in the design of nontoxic, stable and high-performance perovskite derivative for optoelectronics applications.

Keywords: $Cs_2SnCl_{6-x}Br_x$; Tin-based single crystals; Photodetectors

Jun Zhou[#], Jiajun Luo[#], Ximing Rong[#], Peijia Wei, Maxim S. Molokeev, Yang Huang, Jing Zhao, Quanlin Liu, Xiuwen Zhang, Jiang Tang, Zhiguo Xia[*]

Lead-Free Perovskite Derivative $Cs_2SnCl_{6-x}Br_x$ Single crystals for Narrowband Photodetectors

TOC

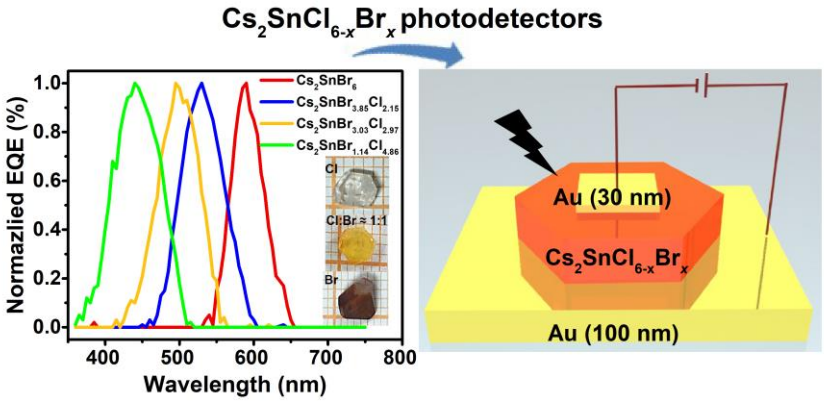

Supporting Information

Lead-Free Perovskite Derivative $Cs_2SnCl_{6-x}Br_x$ Single crystals for Narrowband Photodetectors

Jun Zhou[#], Jiajun Luo[#], Ximing Rong[#], Peijia Wei, Maxim S. Molokeev, Yang Huang, Jing Zhao, Quanlin Liu, Xiuwen Zhang, Jiang Tang, Zhiguo Xia[*]

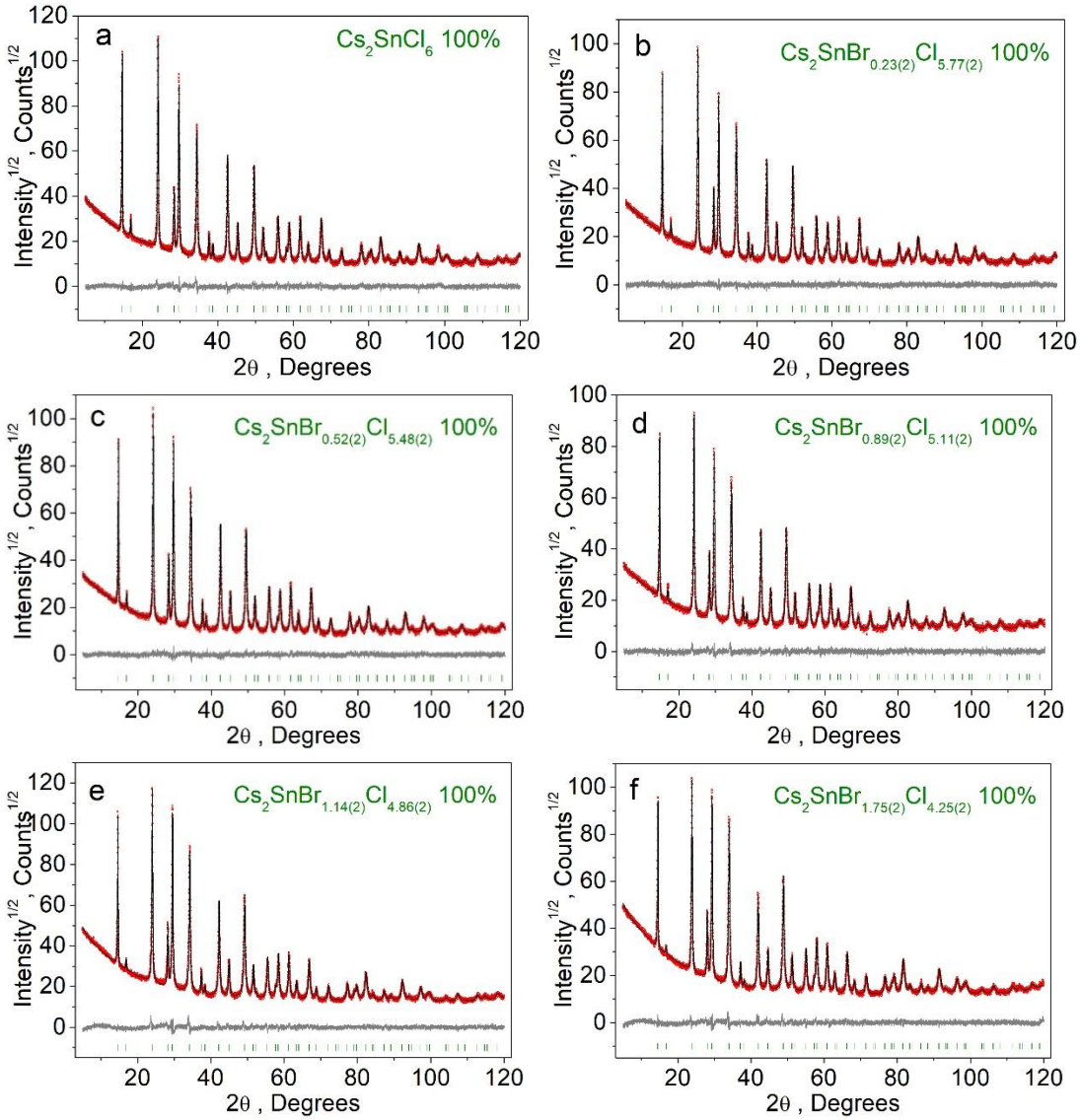

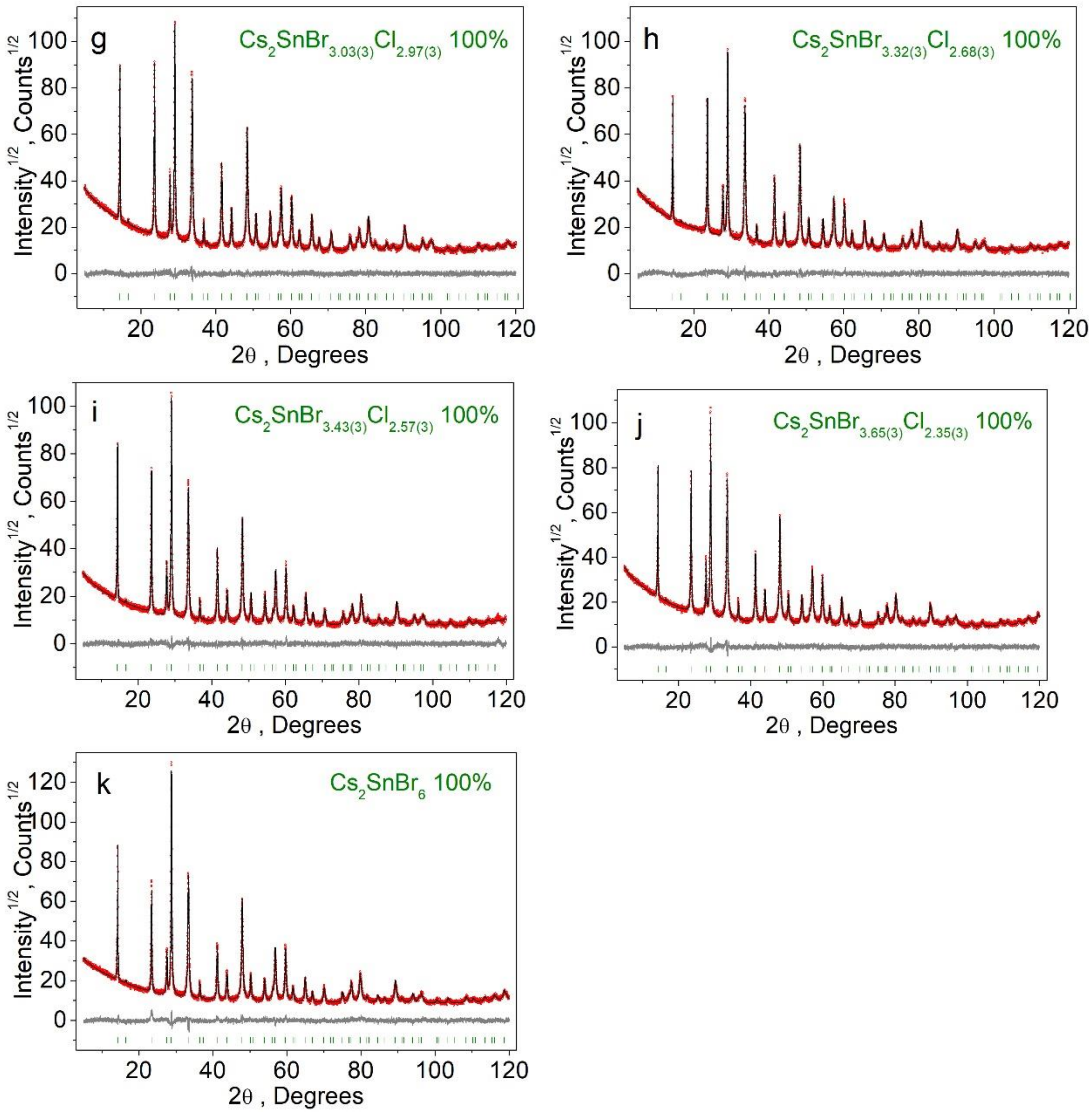

Figure S1. Difference Rietveld plot of $Cs_2SnCl_{6-x}Br_x$: a) x = 0; b) x = 0.23 (2); c) x = 0.52 (2); d) x = 0.89 (2); e) x = 1.14 (2); f) x = 1.75 (2); g) x = 3.03 (3); h) x = 3.32 (3); i) x = 3.43 (3); j) x = 3.65 (3); k) x = 6.

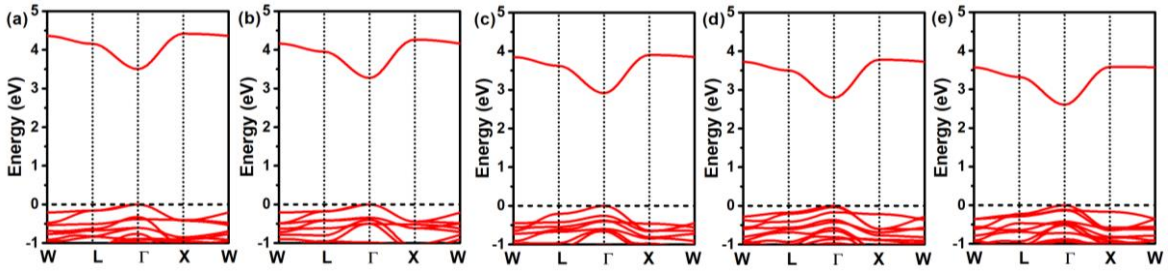

Figure S2. Calculated HSE band structures of $Cs_2SnCl_{6-x}Br_x$: a) x = 1; b) x = 2; c) x = 3; d) x = 4; e) x = 5.

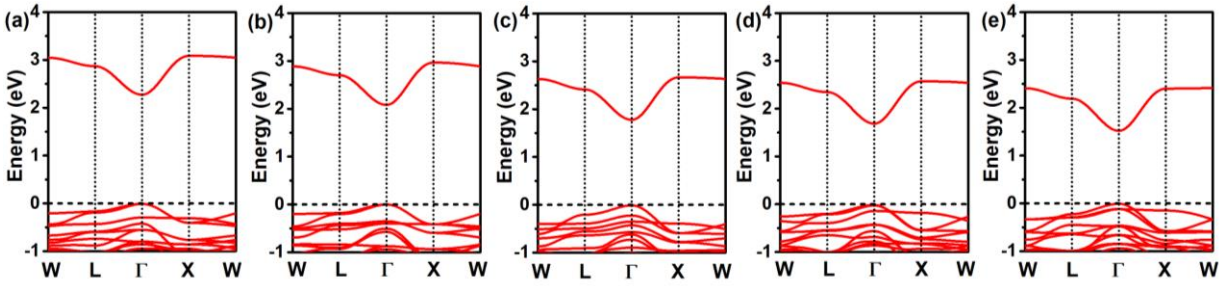

Figure S3. Calculated PBE band structures of $Cs_2SnCl_{6-x}Br_x$: a) x = 1; b) x = 2; c) x = 3; d) x = 4; e) x = 5.

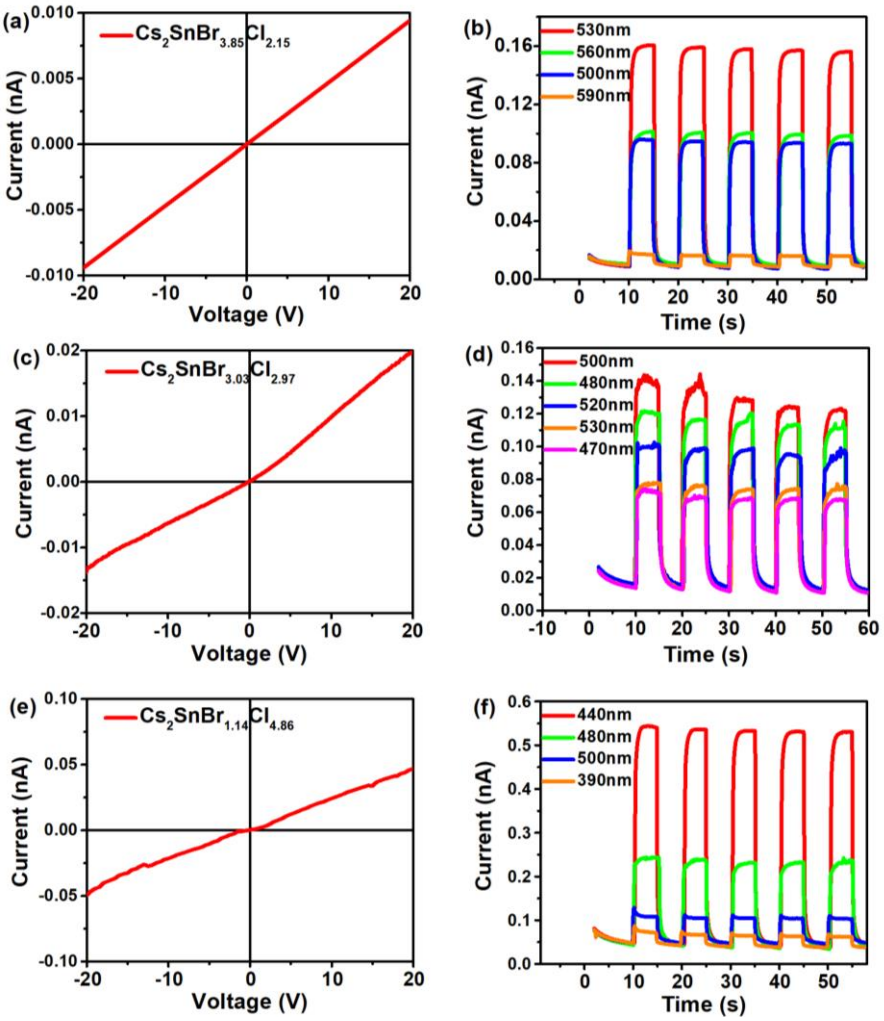

Figure S4. Devices data for crystals with different Cl/Br ratio. a) and b) $Cs_2SnBr_{3.85}Cl_{2.15}$, c) and d) $Cs_2SnBr_{3.03}Cl_{2.97}$, e) and f) $Cs_2SnBr_{1.14}Cl_{4.86}$.

Table S1. Main parameters of processing and refinement of the $Cs_2SnCl_{6-x}Br_x$ samples.

x	Phase	Space group	Cell parameters (º, Å), Cell volume (Å^3)	R_{wp}, R_p, R_B (%), χ^2
0	Cs_2SnCl_6	*Fm*-3*m*	a = 10.3863 (2), V = 1120.41 (5)	6.96, 5.21, 1.57, 1.34

x = 0.23 (2)	$Cs_2SnBr_{0.23(2)}Cl_{5.77(2)}$	*Fm*-3*m*	a = 10.4029 (2), V = 1125.79 (5)	6.81, 4.96, 1.09, 1.16
x = 0.52 (2)	$Cs_2SnBr_{0.52(2)}Cl_{5.48(2)}$	*Fm*-3*m*	a = 10.4179 (2), V = 1130.69 (5)	6.77, 4.99, 1.49, 1.19
x = 0.89 (2)	$Cs_2SnBr_{0.89(2)}Cl_{5.11(2)}$	*Fm*-3*m*	a = 10.4431 (2), V = 1138.92 (6)	7.17, 5.24, 0.74, 1.22
x = 1.14 (2)	$Cs_2SnBr_{1.14(2)}Cl_{4.86(2)}$	*Fm*-3*m*	a = 10.4703 (2), V = 1147.83 (8)	6.39, 4.78, 0.86, 1.51
x = 1.75 (2)	$Cs_2SnBr_{1.75(2)}Cl_{4.25(2)}$	*Fm*-3*m*	a = 10.5430 (2), V = 1171.89 (7)	6.19, 4.71, 1.03, 1.43
x = 3.03 (3)	$Cs_2SnBr_{3.03(3)}Cl_{2.97(3)}$	*Fm*-3*m*	a = 10.6422 (2), V = 1205.30 (6)	6.46, 4.82, 1.20, 0.75
x = 3.32 (3)	$Cs_2SnBr_{3.32(3)}Cl_{2.68(3)}$	*Fm*-3*m*	a = 10.6531 (4), V = 1209.00 (12)	6.81, 5.21, 1.23, 0.81
x = 3.43 (3)	$Cs_2SnBr_{3.42(3)}Cl_{2.57(3)}$	*Fm*-3*m*	a = 10.6496 (2), V = 1207.83 (8)	8.14, 6.07, 1.25, 1.27
x = 3.65 (3)	$Cs_2SnBr_{3.65(3)}Cl_{2.35(3)}$	*Fm*-3*m*	a = 10.6962 (2), V = 1223.73 (8)	7.07, 5.36, 1.24, 0.76
6	Cs_2SnBr_6	*Fm*-3*m*	a = 10.7435 (2), V = 1240.03 (6)	8.89, 6.81, 3.84, 1.50

Table S2. Fractional atomic coordinates and isotropic displacement parameters (Å^2) of $Cs_2SnCl_{6-x}Br_x$

	x	y	z	B_{iso}	occ.
x = 0, Cs_2SnCl_6					
Cs	1/4	1/4	1/4	2.22 (11)	1
Sn	0	0	0	1.45 (11)	1
Cl	0.2326 (2)	0	0	1.50 (11)	1
x = 0.23 (2), $Cs_2SnBr_{0.23(2)}Cl_{5.77(2)}$					
Cs	1/4	1/4	1/4	2.5 (1)	1
Sn	0	0	0	1.6 (1)	1
Cl	0.2338 (2)	0	0	2.2 (1)	0.962 (3)
Br	0.2338 (2)	0	0	2.2 (1)	0.038 (3)
x = 0.52 (2), $Cs_2SnBr_{0.52(2)}Cl_{5.48(2)}$					
Cs	1/4	1/4	1/4	2.6 (1)	1

Sn	0	0	0	1.8 (1)	1
Cl	0.2345 (2)	0	0	2.39 (9)	0.914 (3)
Br	0.2345 (2)	0	0	2.39 (9)	0.086 (3)
			x = 0.89 (2), $Cs_2SnBr_{0.89(2)}Cl_{5.11(2)}$		
Cs	1/4	1/4	1/4	2.18 (12)	1
Sn	0	0	0	1.26 (12)	1
Cl	0.2354 (2)	0	0	2.18 (11)	0.852 (4)
Br	0.2354 (2)	0	0	2.18 (11)	0.148 (4)
			x = 1.14 (2), $Cs_2SnBr_{1.14(2)}Cl_{4.86(2)}$		
Cs	1/4	1/4	1/4	2.08 (12)	1
Sn	0	0	0	1.07 (13)	1
Cl	0.2361 (2)	0	0	1.92 (11)	0.810 (4)
Br	0.2361 (2)	0	0	1.92 (11)	0.190 (4)
			x = 1.75 (2), $Cs_2SnBr_{1.75(2)}Cl_{4.25(2)}$		
Cs	1/4	1/4	1/4	1.86 (12)	1
Sn	0	0	0	0.75 (12)	1
Cl	0.2376 (2)	0	0	1.5 (1)	0.708 (4)
Br	0.2376 (2)	0	0	1.5 (1)	0.292 (4)
			x = 3.03 (3), $Cs_2SnBr_{3.03(3)}Cl_{2.97(3)}$		
Cs	1/4	1/4	1/4	2.26 (11)	1
Sn	0	0	0	1.29 (11)	1
Cl	0.2386 (1)	0	0	2.0 (1)	0.495 (4)
Br	0.2386 (1)	0	0	2.0 (1)	0.505 (4)
			x = 3.32 (3), $Cs_2SnBr_{3.32(3)}Cl_{2.68(3)}$		
Cs	1/4	1/4	1/4	2.22 (13)	1
Sn	0	0	0	1.04 (13)	1
Cl	0.2383 (2)	0	0	1.87 (12)	0.446 (5)
Br	0.2383 (2)	0	0	1.87 (12)	0.554 (5)
			x = 3.43 (3), $Cs_2SnBr_{3.42(3)}Cl_{2.57(3)}$		
Cs	1/4	1/4	1/4	2.40 (14)	1
Sn	0	0	0	1.42 (15)	1
Cl	0.2388 (2)	0	0	2.08 (12)	0.430 (5)
Br	0.2388 (2)	0	0	2.08 (12)	0.570 (5)
			x = 3.65 (3), $Cs_2SnBr_{3.65(3)}Cl_{2.35(3)}$		
Cs	1/4	1/4	1/4	2.07 (13)	1
Sn	0	0	0	1.00 (14)	1
Cl	0.2392 (2)	0	0	1.74 (12)	0.392 (5)

Br	0.2392 (2)	0	0	1.74 (12)	0.608 (5)
			x = 6, Cs_2SnBr_6		
Cs	1/4	1/4	1/4	1.63 (13)	1
Sn	0	0	0	0.46 (13)	1
Br	0.2403 (2)	0	0	2.71 (12)	1

Table S3. Main bond lengths (Å) of $Cs_2Sn(Cl_{1-x}Br_x)_6$

		x = 0, Cs_2SnCl_6	
Cs—Cl	3.6765 (1)	Sn—Cl	2.416 (2)
		x = 0.23 (2), $Cs_2SnBr_{0.23(2)}Cl_{5.77(2)}$	
Cs—(Cl/Br)	3.682 (1)	Sn—(Cl/Br)	2.432 (2)
		x = 0.52 (2), $Cs_2SnBr_{0.52(2)}Cl_{5.48(2)}$	
Cs—(Cl/Br)	3.687 (1)	Sn—(Cl/Br)	2.443 (2)
		x = 0.89 (2), $Cs_2SnBr_{0.89(2)}Cl_{5.11(2)}$	
Cs—(Cl/Br)	3.695 (1)	Sn—(Cl/Br)	2.459 (2)
		x = 1.14 (2), $Cs_2SnBr_{1.14(2)}Cl_{4.86(2)}$	
Cs—(Cl/Br)	3.705 (1)	Sn—(Cl/Br)	2.472 (2)
		x = 1.75 (2), $Cs_2SnBr_{1.75(2)}Cl_{4.25(2)}$	
Cs—(Cl/Br)	3.730 (1)	Sn—(Cl/Br)	2.505 (2)
		x = 3.03 (3), $Cs_2SnBr_{3.03(3)}Cl_{2.97(3)}$	
Cs—(Cl/Br)	3.765 (1)	Sn—(Cl/Br)	2.540 (2)
		x = 3.32 (3), $Cs_2SnBr_{3.32(3)}Cl_{2.68(3)}$	
Cs—(Cl/Br)	3.769 (1)	Sn—(Cl/Br)	2.539 (2)
		x = 3.43 (3), $Cs_2SnBr_{3.42(3)}Cl_{2.57(3)}$	
Cs—(Cl/Br)	3.767 (1)	Sn—(Cl/Br)	2.543 (2)
		x = 3.65 (3), $Cs_2SnBr_{3.65(3)}Cl_{2.35(3)}$	
Cs—(Cl/Br)	3.783 (1)	Sn—(Cl/Br)	2.559 (2)
		x = 6, Cs_2SnBr_6	
Cs—Br	3.7998 (1)	Sn—Br	2.582 (2)

Table S4. Energy difference of $CsPb(Sn)Cl(Br)_3$ and $Cs_2SnCl(Br)_6$ between structures with different space group.

Compound	E_{Pnma} (meV/atom)	$E_{Fm\text{-}3m}$ (meV/atom)
$CsPbCl_3$	0	12.52
$CsPbBr_3$	0	15.00
$CsSnCl_3$	0	2.10
$CsSnBr_3$	0	2.54

Cs_2SnCl_6	0	0.56
Cs_2SnBr_6	0	0.04